Article

Modelling, Analysis and Performance of a Low Inertia AC-DC Microgrid

Mohamed A. Afifi [ID], Mostafa I. Marei *[ID] and Ahmed M. I. Mohamad [ID]

Department of Electrical Power & Machines, Faculty of Engineering, Ain Shams University, Cairo 11517, Egypt
* Correspondence: mostafa_ibrahim@eng.asu.edu.eg

Abstract: In a world where the energy crisis is becoming overwhelming, demand for integrating renewable energy sources is increasing and forming microgrids is becoming an essential solution. The new microgrid systems, which depend mainly on renewable energy sources instead of conventional synchronous generators, come with a low inertia concern. This paper proposes a virtual inertia controller based on a high-pass filter (HPF) to support the frequency of the AC microgrid while maintaining the DC voltage of the DC microgrid within the nominal ranges in cases of contingencies. The proposed system encounters an AC-DC microgrid with a renewable energy source on the DC microgrid alongside constant power load and resistive loads, while on the AC microgrid side, a synchronous generator is used to present the low inertia of the grid with dynamic loads and static loads. The state-space linearized model of the system is developed and verified using Matlab Simulink. The dynamic response of the proposed controller is compared to the low-pas filter (LPF)-based controller. Moreover, the effect of changing the system's parameters on eigenvalues is investigated.

Keywords: microgrids; induction motor; stability; dynamic loads; low inertia; frequency support; virtual inertia

1. Introduction

The inertia constant of the microgrid is determined by its total rotating kinetic energy [1]. Distributed generators based on non-spinning power electronics would greatly reduce the system's overall inertia coefficient as a result of the widespread use of renewable energy sources such as solar power. Smart grid systems are susceptible to network disturbances because of the low inertia of their inverter systems [2]. The rate of change of frequency (RoCoF) is the most important parameter that is used in the loss of mains protection relays, as an oscillation between 1.5 to 2 Hz/s may lead to relay tripping and may result in cascaded failures of the generating units and hence a blackout [3]. Studies show that the RoCoF and the frequency nadir are indicators of the system's inertia [4]. In the traditional power systems, this issue was not significant as the synchronous machines' inertia limited the RoCoF and prevented tripping; however, on increasing the penetration level of renewable energy sources into the grid, the overall system inertia is decreased and the RoCoF needs to be monitored [5,6]. The inertia emulation is the virtual inertia at which the converters contribute to the physical synchronous generators' inertia resulting from their kinetic energy stored in the rotors to maintain the grid frequency [7]. In order to keep frequency excursions within the bands in [8], the grid regulations stipulate that the power balance between generation and demand must be established as quickly as possible after a frequency disturbance. The primary control mechanism during a frequency event has to halt the rapid frequency drop, or frequency nadir, within a period of a few seconds. Then, after a few minutes, the secondary control brings the frequency back to normal, the droop and the inertia control are contained within the primary control loop [8]. Recent studies show that the DC-link voltage could be allowed to vary to distribute virtual inertia through grid-connected converters as described in [9]. This is accomplished by

connecting the reference voltage of the DC bus to the system frequency. A new technology called Distributed Virtual inertia (DVI) was implemented in [7]; this technology aims to increase the inertia of the future power grids where many grid-connected converters would be utilized to interface the renewable energy sources. In this study, the capacitors used on the DC side of each converter are utilized as energy storage to produce virtual inertia during contingencies. This approach will reduce the cost of new installations by utilizing the installed converters. In contrast, virtual synchronous generators (VSGs) or virtual synchronous machines (VSMs) are different because they produce virtual inertia by using a control loop to mimic the behaviour of synchronous generators [10]. Recent studies of the applications and future trends of virtual synchronous generators along with fundamentals, different topologies and a detailed structure of the VSG can be found in [11,12]. Strategies for controlling the grid-connected inverter to function as a synchronous generator are introduced in [13]. Although the synthetic virtual inertia value may be altered by adjusting the control settings, a high power rating of the power converter and extra energy storage units are required. However, the possibility of inconsistency in the input and output power of the converters under VSG control is a concern. Because power converters cannot handle power imbalances like synchronous generators by absorbing or delivering the required kinetic energy, an energy storage device such as batteries is always necessary to provide power control in VSG. However, it was assumed that the VSG has no limitations over the power that can be given or absorbed, which needs more experimental studies to be proven. The energy storage systems must be adequately designed in accordance with the VSG to produce the desired inertial response, which will result in system complexity [14]. The value of DC link capacitances would limit the virtual inertia of the VSGs if no energy storage systems were used. Battery Energy Storage Systems (BESSs) can be used to support the frequency while the grid frequency fluctuates. The battery will often oscillate between charging and discharging status, resulting in a decreased lifespan and system efficiency. This becomes the most significant disadvantage of utilizing BESSs alone [15]. However, new studies proposed new technologies that offer accurate monitoring of the state of health of lithium-ion batteries, allowing energy storage systems to play an essential role in the inertial support [16]. In [17], the sizing of the battery system required to emulate the virtual inertia is studied and a guideline was provided on how to match the VSM parameters with the energy storage system. High-power-density capacitors or ultracapacitors enable rapid charge and discharge. Because of the differences in the properties of batteries and capacitors [18], they may both be used in VSMs, where batteries counterbalance the long-term power needed by the droop control. Capacitors/ultracapacitors can support short-term power needed in inertia emulation; however, the emerging technologies of the ultracapacitors have yet to be commercialized [18]. Although the VSMs that adopt hybrid energy storage systems have been validated, they still need authorization to be utilized in the power grid. As a result, the VSM is an emerging rather than a tested and commercialized approach. Although employing synchronous condensers linked to the grid is a well adopted approach, it is only a second option for inertia augmentation owing to the high costs [19]. The DC grid poses a high potential for frequency support. DC grids can control and integrate distributed energy resources into power networks and provide services to AC systems, such as voltage and frequency support. This can be accomplished by regulating the interconnecting converters and the connected distributed energy resources. At the high and medium voltage levels [20], offshore wind farms are connected to the AC grids through high voltage DC (HVDC) and multiterminal DC (MTDC) networks based on VSC technology to increase operational flexibility and supply security [21]. On the other hand, adding more wind farms leads to a reduction in inertia. In [22], an adaptive droop control strategy is adopted such that the VSC-based (MTDC) method provides inertial support to the onshore AC microgrid system depending on the support from offshore wind turbines through an HVDC line. Numerous solutions were proposed in [22] for HVDC/MVDC systems to enable inertia emulation control algorithms, where the energy stored in the DC link capacitors was used to emulate the inertial response of a synchronous

generator. Using the DC voltage of the MTDC grid, onshore converter stations can use wind farms' power for frequency support. A voltage-frequency droop was defined for offshore wind farm converter stations and an active power-frequency droop for doubly fed induction generator (DFIG) converters. A communication-less approach which was previously implemented is used in [23]. However, it is used with communication which depends on a fibre optic cable to quickly communicate the frequency errors to the offshore converters. In high voltage direct current (HVDC) transmission systems, the transients are often separated intentionally to contain instabilities within one system and prevent instabilities from affecting other connected systems. In [24], a novel approach is presented to utilize the capacitance of the HVDC lines to provide inertial support by allowing a permissible variation in the DC voltage. Another adaptive technique which did not need communication is presented in [22]. At the low voltage level, the DC–AC converter was controlled as a virtual synchronous machine, providing inertia during the AC and DC side disturbances and offering reserve to the grid [25]. Additionally, a decentralized droop control technique was employed for rapid active power regulation and increased system frequency support within the DC microgrid in [26]. Moreover, a virtual admittance approach was used to improve the voltage profile in the local DC microgrid during AC frequency DC fault events [26]. Various studies focused on control techniques for DC grid characteristics such as power-sharing, local voltage stability and energy management within microgrid bounds. Wind turbines, photovoltaic (PV) and energy storage were previously explored to provide frequency support [27]. However, only a few studies have examined the feasibility of employing a DC distribution system to support the AC grid frequency, considering the detailed dynamics of both DC and AC grids [28]. Previous studies presented a microgrid model based on the data collected from field data of an existing microgrid; the model was verified to produce an accurate response compared to the existing microgrid and was used to study the response in the case of symmetrical fault [29]. Therefore, it is essential to examine the dynamic performance of the hybrid AC/DC system, considering both grids' detailed dynamics and the control methods required to mitigate any adverse impact that could affect the stability of the entire system.

The paper's contributions to the field can be summarized as follows:

1. This paper presents a comprehensive modelling of an AC-DC microgrid considering the interlinking voltage source converter equipped with an inertial support loop, the DC link dynamics, AC grid load modelling and synchronous generator dynamics (governor and the AVR dynamics).
2. A new virtual inertia controller based on a high-pass filter (HPF) compensator is proposed and its dynamic performance is compared with the low-pass filter (LPF)-based virtual methods used in the literature; the advantages of the proposed method are highlighted, showing the differences between the two controllers.
3. Using eigenvalue-based analysis, a stability analysis is provided to study the impact of the system parameters' uncertainty on the entire system stability to demonstrate the interaction dynamics that arise after adding the virtual inertia loop.
4. Finally, time domain simulations and performance check of the proposed method are presented, considering different operating scenarios.

The paper is organized as follows; Section 2 introduces the utilized system's model. In Section 3, a stability study of the effect of varying system parameters is performed. In Section 4, simulation results are depicted; first, the linearized state space model is verified compared to the results from Matlab Simulink and the results of the proposed controller are presented. In Section 5, the paper is concluded.

2. System Model

The microgrid under study represents a typical model used for oil and gas companies in Egypt in areas remotely far from the grid. This microgrid is based mainly on synchronous generators with motor loads and some static loads. Recently, renewable energy sources have been installed and integrated into the microgrid. A typical site in the eastern desert of

Egypt is energized by nine synchronous generators which share the loads equally using the droop control. A similar model has been used in this paper to represent the dynamics of a typical oil and gas site. Additionally, a DC microgrid formed from nearby renewable energy resources is employed to support the AC grid loads.

Figure 1 depicts the microgrid system under study. The system consists of a diesel generator, static loads and induction motor loads. The loads and sources are connected to the Point of Common Coupling (PCC) of the AC microgrid. The DC microgrid is connected through a VSC, which is controlled by virtual inertia loop, to the AC grid.
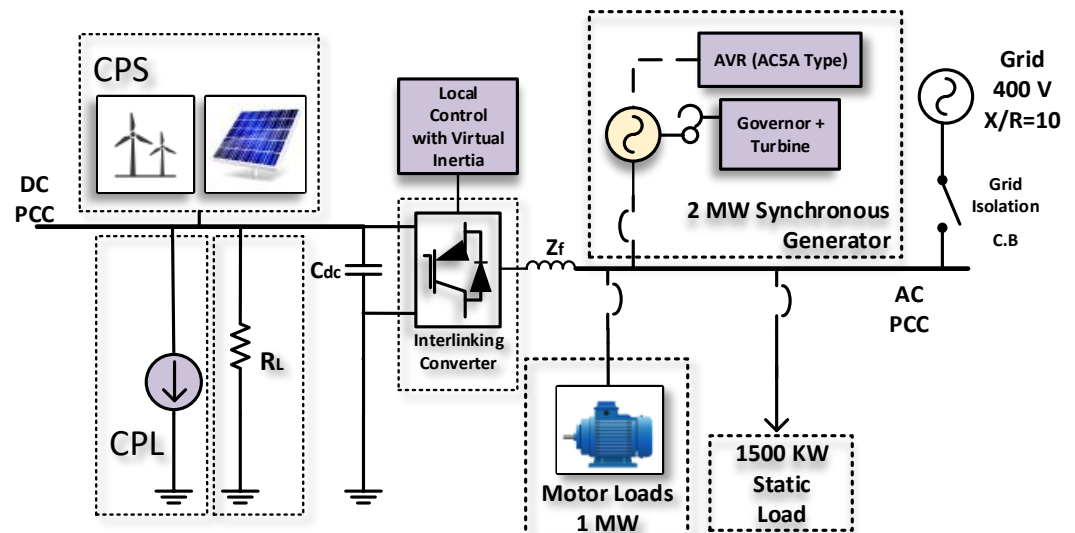

Figure 1. Microgrid system under study.

The DC microgrid consists of a constant power source representing renewable energy sources, such as a PV or wind system. The DC loads are modelled as constant power loads to represent the tightly regulated loads and a resistance (RL), representing the resistive loads on the DC grid side. The diesel generator unit maintains the system voltage and frequency and shares the total load demand with the VSC when the AC grid setup operates in autonomous mode. The system shown in Figure 1 is employed to study the frequency response of the microgrid in terms of RoCoF and nadir, as well as how the DC voltage of the DC microgrid is affected during any contingency on the AC side. Moreover, the dynamic performance of the proposed virtual inertia controller for frequency support is investigated on the system of Figure 1. A small-signal state-space model of the microgrid's components was built to test the system's stability and study the effect of parameters changing on the response, which will be presented in the following subsections.

2.1. Voltage Source Converter Model

The VSC interfaces the DC microgrid with the AC microgrid under investigation. Moreover, the VSC control contributes to the microgrid's stability in cases of contingency by supporting the microgrid frequency in terms of rate of change of frequency (RoCoF) and nadir by providing virtual inertia support. The VSC supports the microgrid frequency by reflecting the dynamics of the frequency to the DC voltage bus through an inertial gain and either a high-pass filter (HPF) or a low-pass filter (LPF). The results of the two methods are introduced in the following sections to compare dynamic behavior and performance.

The total power injected by the DC microgrid to support the AC side is given as (P_{ex}); it is the result of subtracting the constant power source and the constant power load (P_{CPL}) as well as the resistive load in the DC microgrid side while the power transferred to the AC

microgrid is given by (P_s). Equation (1) represents the dynamics of the DC link capacitor (C_{dc}) of the interlinking VSC.

$$\frac{1}{2}C_{dc}V_{dc}^2 = P_{ex} - P_s. \tag{1}$$

Ignoring the VSC losses, the power injected into the AC microgrid is defined in (2), where V_d, V_q are AC grid voltages in the DQ reference frame and I_d, I_q are the VSC output currents of the VSC in the DQ reference frame.

$$P_s = V_d\,I_d + V_q\,I_q. \tag{2}$$

The renewable energy resources in the DC microgrid can be modelled as a constant power source with power P_{DG}, injecting a constant power into the AC grid, where the DC grid voltage is regulated via the interlinking VSC. This action is due to the slow power variation nature of the renewable energy resources compared to the inertia support loop. The DC microgrid resistive loads are modelled as a resistance R. Therefore, the excess power available from the DC microgrid can be calculated as follows:

$$P_{ex} = P_{DG} - P_{CPL} - \frac{V_{dc}^2}{R}. \tag{3}$$

The Equations (4a)–(4c) describe the dynamics of the VSC control loop shown in Figure 2, where τ_i is the time constant of the closed loop current controller, k_p, k_i are the DC link voltage controller gains, I_{dVSC}^*, I_{qVSC}^* are the reference values of the currents in the DQ frame. For unity power factor operation, the q-reference current is set to zero.

$$I_d = \frac{I_d^*}{\tau_i s + 1}, \tag{4a}$$

$$I_q = \frac{I_q^*}{\tau_v} - \frac{I_q}{\tau_i}, \tag{4b}$$

$$I_d^* = \frac{1}{1.5\,V_d}\left(\left(k_p + \frac{k_i}{s}\right)\left(V_{dc}^{2*} - V_{dc}^2\right) + P_s\right). \tag{4c}$$
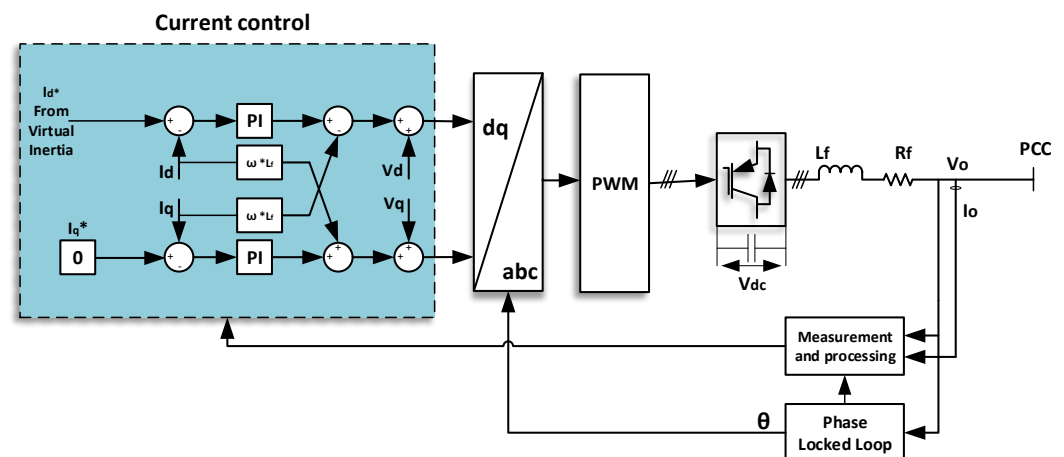

Figure 2. Control of the VSC.

Figures 3 and 4 show the proposed virtual inertia controller using an HPF $G_{HPF(s)}$ and LPF controller $G_{LPF(s)}$, respectively. The results of both controllers are compared in the Simulation results section. The equations that describe the virtual inertia loop are given in Equations (5a) and (5c) for the HPF and LPF methods, respectively.

$$V_{dc}^* = V_{dcref}^* + K * G_{HPF(s)}\omega_s, \tag{5a}$$

$$G_{HPF(s)} = \frac{s}{s + \omega_{HPF}}, \tag{5b}$$

$$V_{dc}^* = V_{dcref}^* + K * G_{LPF(s)}(\omega^* - \omega_{meas}), \tag{5c}$$

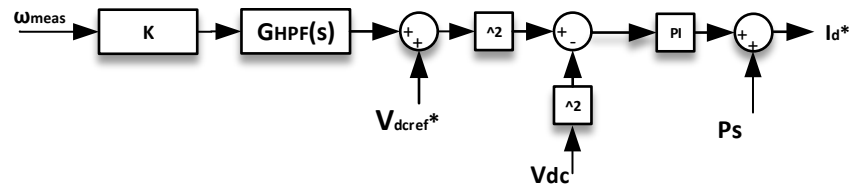$$G_{LPF(s)} = \frac{\omega_{LPF}}{s + \omega_{LPF}}. \tag{5d}$$

Figure 3. Proposed Virtual Inertia Loop based on HPF.
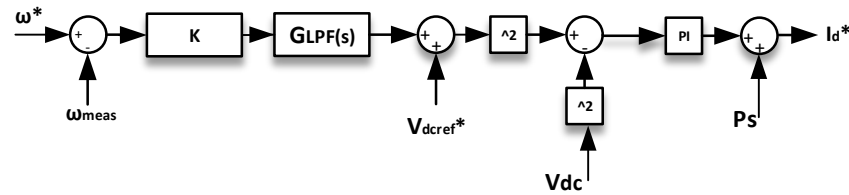

Figure 4. Virtual Inertia Loop based on LPF.

2.2. Model of Induction Machine

The relationship between the stator and rotor voltages and currents of the IM in the rotating reference frame is given in (6). It is possible to write the IM equations using any of the fluxes and currents as the state variable (noting that they are not independent variables). However, using currents as state variables is preferable for integrating IM state equations into the whole microgrid state-space model. Hence, the relationship between the stator and rotor voltage and current is expressed as follows in the common synchronous DQ reference frame [30]:

$$V_{qs} = R_s \, I_{qs} + L_s i_{qs} s + L_m i_{qr} s + w_r L_s I_{ds} + w_r L_m I_{dr}, \tag{6a}$$

$$V_{ds} = R_s \, I_{ds} + L_s i_{ds} s + L_m i_{dr} s - w_r L_s I_{qs} - w_r L_m I_{qr}, \tag{6b}$$

$$V_{qr} = R_r \, I_{qr} + L_r i_{qr} s + L_m i_{qs} s + (w_s - w_r) L_r I_{dr} + (w_s - w_r) L_m I_{ds}, \tag{6c}$$

$$V_{dr} = R_r \, I_{dr} + L_r i_{dr} s + L_m i_{ds} s - (w_s - w_r) L_r I_{qr} - (w_s - w_r) L_m I_{qs}, \tag{6d}$$

where L_s and L_r represent the stator and rotor inductance. While R_s and R_r represent the stator and rotor resistance; Lm and ωr, represent the mutual inductance and rotor speed, respectively. The electromagnetic torque is formulated as follows:

$$T_e = \frac{3}{2} * \frac{\rho}{2} L_m \left(I_{qs} I_{dr} - I_{ds} I_{qr} \right). \tag{7}$$

The relationship between torque and mechanical speed may be determined using motor slip s and ω_r as follows:

$$(T_e - T_m) * \frac{\rho}{2J} = \omega_r s. \tag{8}$$

In (7) and (8), ρ, J and Tm represent the number of poles, combined motor and load inertia and the load torque, respectively.

2.3. Model of Diesel Generator

2.3.1. Generator Model

The employed AC microgrid model includes the model of a diesel generator, the governor and the automatic voltage regulator (AVR) dynamics. The synchronous generator is modelled such that ω_s is the synchronous speed. The deviation of rotor speed from synchronous speed is defined as $\Delta\omega_{pu}$. I_d, I_q, I_o and $V_{dterm}, V_{qterm}, V_{oterm}$ are the stator currents and the stator voltage in $dq0$ reference frame, respectively. The stator fluxes in the $dq0$ reference frame are defined as ψ_d, ψ_q, ψ_o. E'_d, E'_q, ψ'_d and ψ'_q represent per-unitized versions of the rotor fluxes and E_{fd} is the input field voltage from exciter and P_{mech} is the input mechanical power from the turbine. The per-unit model constants are listed in Table 1. The equations that model the diesel generator are as follows [31,32]:

Table 1. Parameters of the Synchronous Generator.

Parameter	Value (pu)	Parameter	Value (pu)
H	1.5	D	1.33
R_s	0.0095	X_d	2.11
X'_d	0.17	X''_d	0.13
X_q	1.56	X'_q	1.56
X''_q	0.23	x_l	0.05
T'_d	4.4849	T''_d	0.0681
T_q	$0.33 * 0.00001$	T''_q	0.1

$$E''_d = E'_d \frac{x''_q - x_l}{x'_q - x_l} + \psi'_q \frac{x'_q - x''_q}{x'_q - x_l}, \tag{9a}$$

$$E''_q = E'_q \frac{x''_d - x_l}{x'_d - x_l} + \psi'_d \frac{x'_d - x''_d}{x'_d - x_l}, \tag{9b}$$

$$\psi_d = -I_d X''_d + E''_q, \tag{9c}$$

$$\psi_q = -I_q X''_d - E''_d, \tag{9d}$$

$$V_{dterm} = E''_d (1 + \Delta\omega_{pu}) - R_s I_d + X''_q I_q, \tag{9e}$$

$$V_{qterm} = E''_q (1 + \Delta\omega_{pu}) - R_s I_q - X''_d I_d, \tag{9f}$$

$$s\delta = \Delta\omega_{pu} * \omega_s, \tag{9g}$$

$$2Hs\omega = \frac{Pmech - D\omega}{1 + \Delta\omega_{pu}} - (\psi_d I_q - \psi_q I_d), \tag{9h}$$

$$T'_{do} s E'_q = E_{fd} - E'_q - (X_d - X'_d) * \left(I_d - \frac{X'_d - X''_d}{(X'_d - X_l)^2} \left(\psi'_d + (X'_d - X_l) I_d - E'_q \right) \right), \tag{9i}$$

$$T'_{qo} s E'_d = -E'_q - (X_q - X'_q) * \left(I_q - \frac{X'_q - X''_q}{(X'_q - X_l)^2} \left(-\psi'_q + (X'_q - X_l) I_q - E'_d \right) \right), \tag{9j}$$

$$T''_{do} s \psi'_d = -\psi'_d - (X'_d - X_l) I_d + E'_q, \tag{9k}$$

$$T''_{qo}s\psi'_q = -\psi'_q - \left(X'_q - X_l\right)I_q + E'_d, \tag{9l}$$

2.3.2. Governer and Engine Model

The governor and turbine are modelled such that the generator has a droop gain of K_{droop}; to represent the power-sharing in case of multiple generators, the throttle actuator and the engine are modeled via a low-pass filter, each having a time delay of T_1 and T_2, respectively, as follows [31]:

$$P_{mech} = G_{Turbine}(s)G_{Governer}(s)(\omega_{Load} + K_{droop}\Delta\omega), \tag{10a}$$

$$G_{Governer}(s) = \frac{1}{T_1 s + 1}, \tag{10b}$$

$$G_{Turbine}(s) = \frac{1}{T_2 s + 1}. \tag{10c}$$

2.3.3. AVR Model

The AVR is modelled according to the IEEE AC5A type shown in Figure 5 such that the voltage regulator gain $K_A = 100$ and the time constant $T_A = 0.02$, the exciter gain $K_E = 1$ and the time constant $T_E = 0.02$, the damping filter gain $K_F = 0.03$ and the time constants $T_{F1} = 1$, $T_{F2} = 0$, $T_{F3} = 0$ and the field voltage E_f is given by

$$E_f = G_{AVR1}(s)G_{AVR2}(s)(V_t^* - V_t). \tag{11}$$
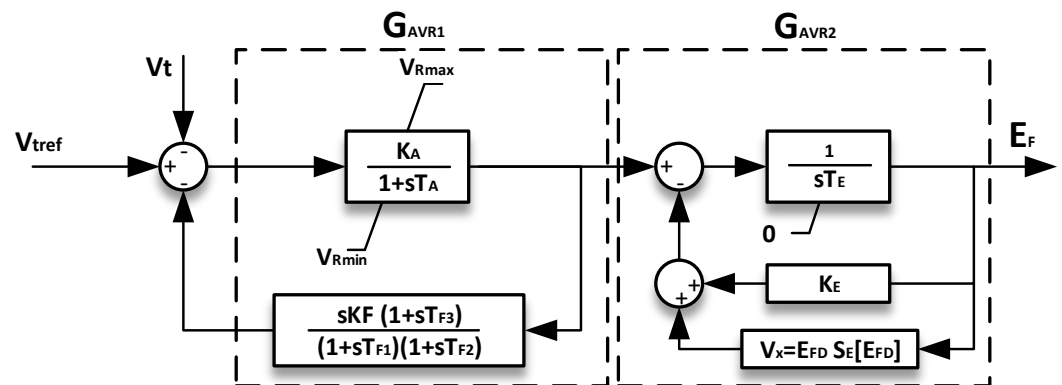

Figure 5. AVR Model.

3. Stability Analysis

The Equations (1)–(11) describing each part of the system are transferred into the state space model using the method detailed in [30,33]. The entire system stability is studied using the eigenvalues of the state space matrix (A) in (12).

$$\dot{\tilde{X}} = A\tilde{X} + B\tilde{U}, \tag{12a}$$

$$\tilde{Y} = C\tilde{X} + D\tilde{U}. \tag{12b}$$

This section examines the system's stability while changing different network parameters. The proposed HPF controller is included in the following cases. The parameters shown in Table 2 are considered the base case and in the subsequent stability analysis, the parameters are varied based on the nominal values in the table. The eigenvalues of the entire system are shown in Table 3.
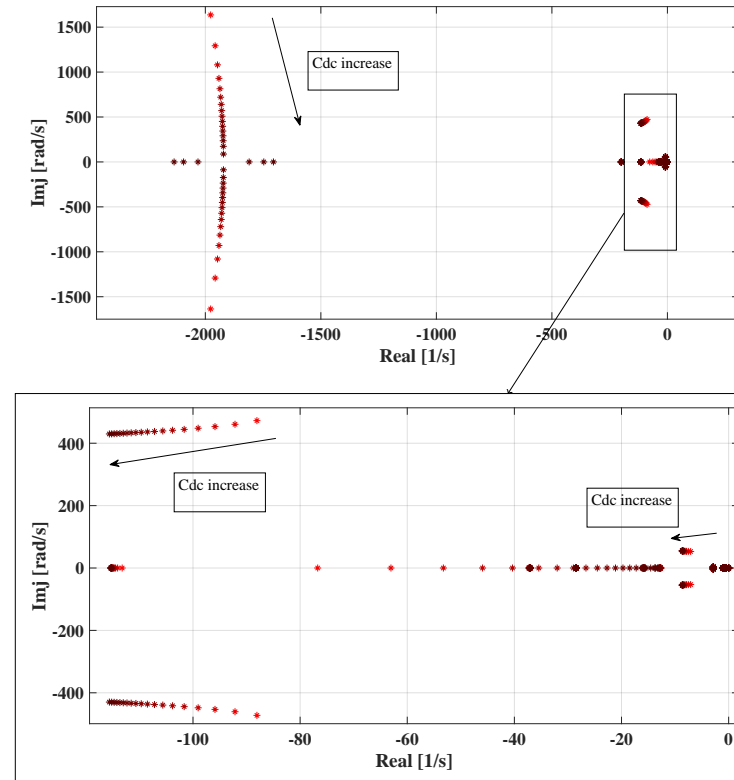
Table 2. The proposed control system parameters.

Parameter	Value	Parameter	Value
AC Grid Rated voltage	400 V	DC microgrid Resistive Load Rdc	0.5 MW
AC Grid Rated Power	2 MVA	Current controller bandwidth $1/\tau_i$	2000
Rated angular frequency	$2\pi * 50$	DC bus capacitance Cdc	0.012 F
Base impedance	$0.4^2/2$	HPF corner frequency	$2\pi * 5$ rad/sec
DC Link Voltage controller gain: kpc, kic	1.75, 50	HPF gain	$5 * 1800 * 6$
DC Bus voltage	1800 V	LPF corner frequency	$2\pi * 5$ rad/sec

Table 3. Eigenvalues of the system.

λ_i	Eigenvalues	λ_i	Eigenvalues
1, 2	$-1927.6 \pm 508.57i$	13	-12.773
3, 4	$-108.51 \pm 436.31i$	14, 15	$-2.8705 \pm 2.8075i$
5	-199.38	16, 17	$-0.83376 \pm 1.4659i$
6	-115.12	18	-4.0322×10^{-13}
7, 8	$-8.6252 \pm 54.647i$	19	-0.94987
9	-37.117	20	-1.1079
10	-28.439	21	-3.0303×10^5
11	-26.636	22	-0.4899
12	-15.862		

3.1. Impact of Cdc Variation

Figure 6 shows the system's eigenvalues while varying the DC link capacitance from 0.2 to 2 of the nominal value. The eigenvalues show the stability effect added to the system and the reduced frequency oscillations by increasing the capacitance, as the capacitance works as the inertia storage for the proposed virtual inertia controller.

Figure 6. Eigenvalues with varying Capacitance.

3.2. Impact of DC Loading Variation

Figure 7 shows the dominant eigenvalues of the system by varying the DC loading from 0.5 to 2 MW. It is obvious that the poles around the origin are shifted towards the

left, increasing the system damping and hence the stability, while the poles representing the DC microgrid system model slightly moved to the right because of the decrease in the resistance and consequently the decrease in the damping of the system. However, the overall effect of the poles is more damped.
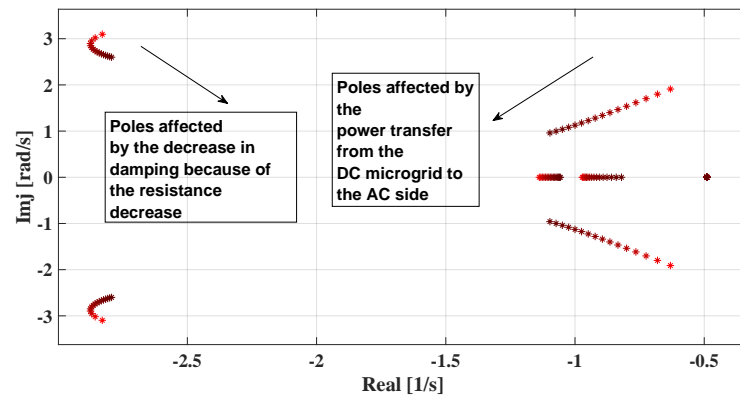

Figure 7. Eigenvalues with varying DC loading.

3.3. Impact of Generator Inertia Variation

Figure 8 shows the dominant poles with the changing in the generator inertia from 0.8 to 1.5 of the nominal value. The poles moved towards the left and produced a more stable response as the synchronous generator inertia is the only source of traditional inertia in the proposed microgrid system.

Figure 8. Eigenvalues with varying generator inertia.

3.4. Impact of AC Loading Variation

The eigenvalues of the system are shown while varying the AC loading ratio between the motor dynamic loading and the static loading, while keeping the total AC system loading constant. The eigenvalues of the AC microgrid are shown in Figure 9. It is clear

that the system depicts a more stable behavior as the dynamic loads or motors increase as it adds more inertia to the system.
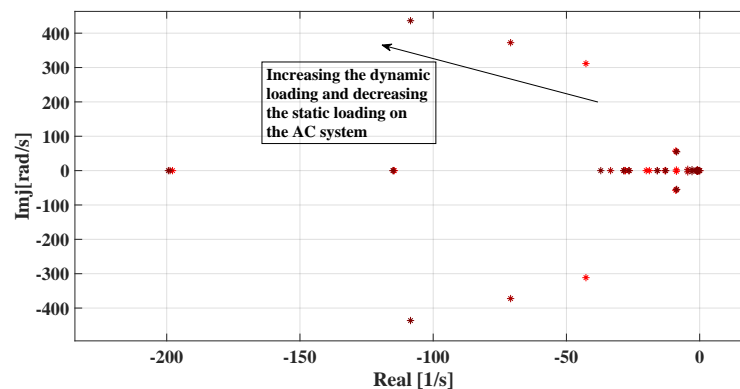

Figure 9. Eigenvalues with varying static AC loading.

3.5. Impact of Inertial Loop Gain Variation

The gain of the HPF-based controller is varied from 0 to approximately infinity to examine the controller's stability. Figure 10 depicts the stable operation of the proposed controller over a wide range of gain values. By increasing the inertia gain of the controller, the system produces an overdamped frequency response with a very high settling time for values of gain values more than 10 pu. From this analysis, the optimum value of the inertia gain is estimated as 3.5 pu, where the damping ratio of the dominant eigenvalues is maximized.

Figure 10. Eigenvalues with varying Kw inertial gain

4. Simulation Results

The dynamic response of the proposed controller and its small signal state space model is implemented using Matlab Simulink software package. In the following subsections,

the small signal model is verified and compared with the Simulink results. Moreover, the dynamic response of the proposed HPF-based controller for virtual inertia is compared with the LPF and relevant cases are simulated to examine the HPF controller. The proposed control system parameters are listed in Table 2.

4.1. Model Verification

Figure 11 depicts the dynamic response of the proposed system using the Simulink nonlinear model and the linearized small-signal state-space model under the same conditions and operating point. The VSC is controlled by the virtual inertia loop based on the HPF and the contingency is introduced on the AC side by increasing the load torque of the induction machines by 3%. The grid frequency and DC link voltage responses verify that the system produces identical results when either the state-space model or the non-linear model is used. When the operating point stays close enough to the linearization point, the results show that the two models well depict both the fast and slow transients in the system. This result shows that the linearized model is valid around the steady state operating point and can be used with conventional linear system analysis methods to evaluate system stability and study the impact of parameter variations.
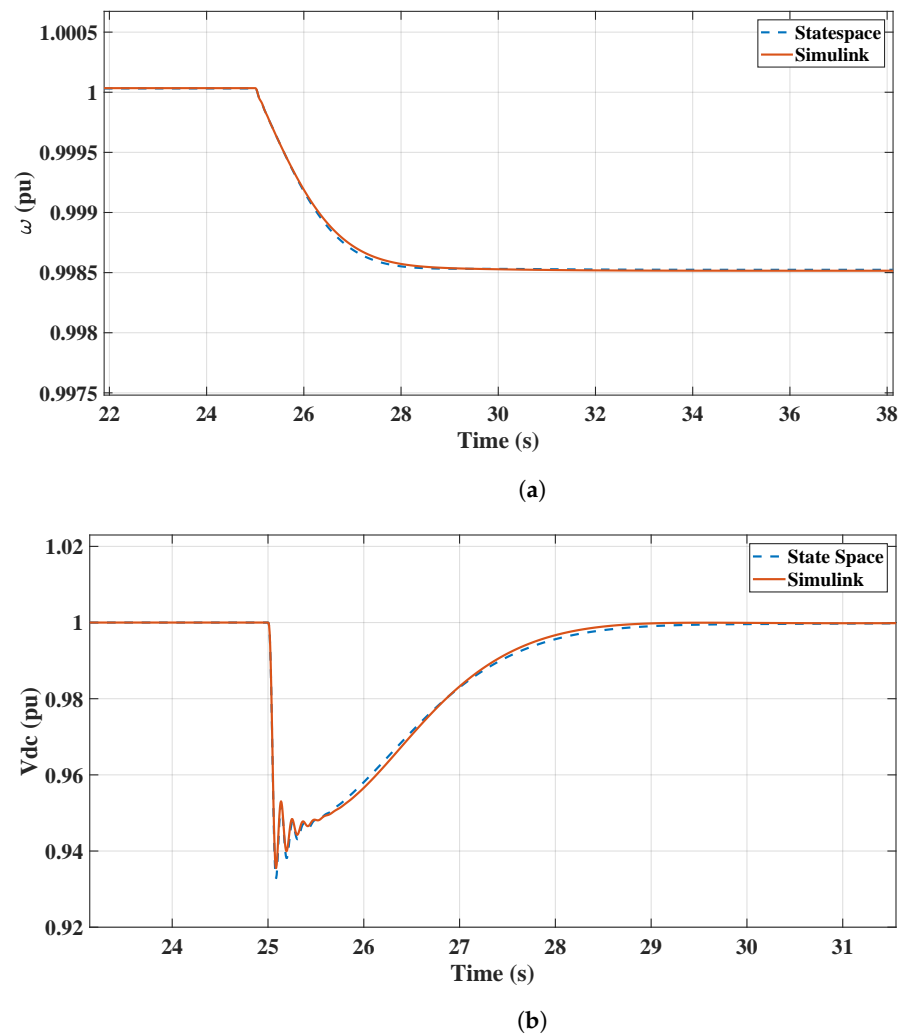

(a)

(b)

Figure 11. Model validation: (**a**) frequency, (**b**) DC link voltage.

4.2. Comparison between LPF- and HPF-Based VI Controllers

This case study is dedicated to comparing the dynamic performance of the proposed control system based on HPF to produce virtual inertia with a scheme based on LPF. The two controllers are tuned to have the same damping coefficients by setting their gains.

The poles responsible for the controller are tuned to have the best possible damping in each controller. Finally, the two controllers are compared together under the same conditions of contingency by increasing the load torque of the motor load by 3% in the AC microgrid side.

Figure 12a shows the frequency response of the AC microgrid, which indicates relatively low-frequency oscillations when LPF is used. However, the frequency stabilizes with a lower steady state error compared to the HPF, which did not encounter high-frequency oscillations. Moreover, Figure 12b demonstrates that the generated inertial response for frequency support comes at the cost of the DC link voltage; in the case of LPF, the DC microgrid voltage is reduced below its nominal value. In contrast, the proposed controller based on HPF results restores the DC link voltage to its nominal value after providing the required inertial support without utilizing a secondary control loop. It is worth mentioning that both the HPF and LPF controllers damp the frequency oscillations compared to the case of disabling the inertia loop.
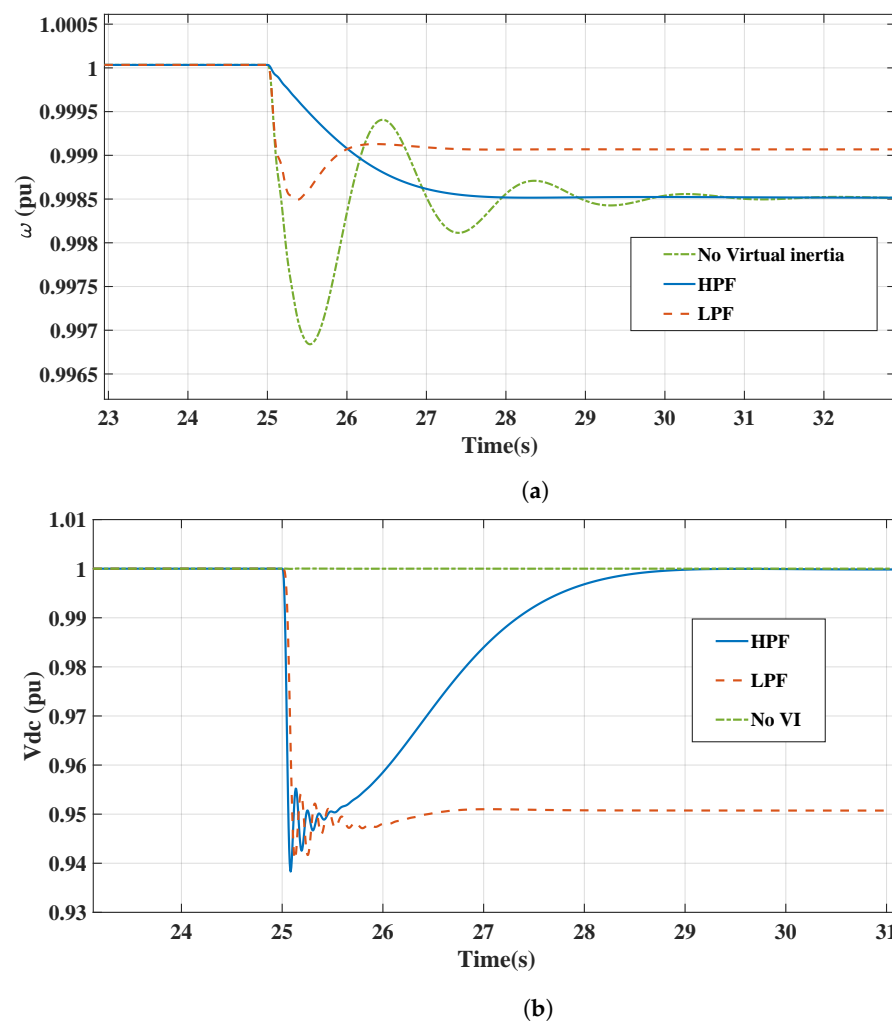

(a)

(b)

Figure 12. Comparison between LPF- and HPF-based controllers for virtual inertia loop: (**a**) Frequency response, (**b**) DC link voltage response.

4.3. Dynamic Loading Effect

The system performance is evaluated under the condition of increasing the voltage of the AC grid by 3% to evaluate the proposed controller in two cases: the AC microgrid with no significant dynamic loads and the case of adding the dynamic loads. In addition, both cases are evaluated when disabling the proposed VI controller. A summary of the results is given in Table 4, where the RoCoF and the nadir of each case are listed. The proposed virtual inertia controller succeeds in enhancing the dynamic response of the two loading

conditions. It can be observed that the nadir is increased at static loading compared to the dynamic loads either when the VI control loop is enabled or disabled. This action is expected as the motors add inertial response to the grid. In addition, the virtual inertia controller enhances the RoCoF and nadir in cases of dynamic loads greater than static loads (See Figure 13). The results show the effect of adding the HPF and the virtual inertia control loop on the frequency response in the contingency case; when the virtual inertia loop is activated, the system produces a better frequency response. It is obvious that the dynamic loads added more inertia to the AC microgrid and hence supported the microgrid and created better frequency. The DC voltage of the DC microgrid is plotted in Figure 14. Finally, Figure 15 depicts the dynamic response of the proposed virtual inertia controller when increasing the load torque of the dynamic loads by 3%.

Table 4. Frequency comparison in different cases of HPF controller.

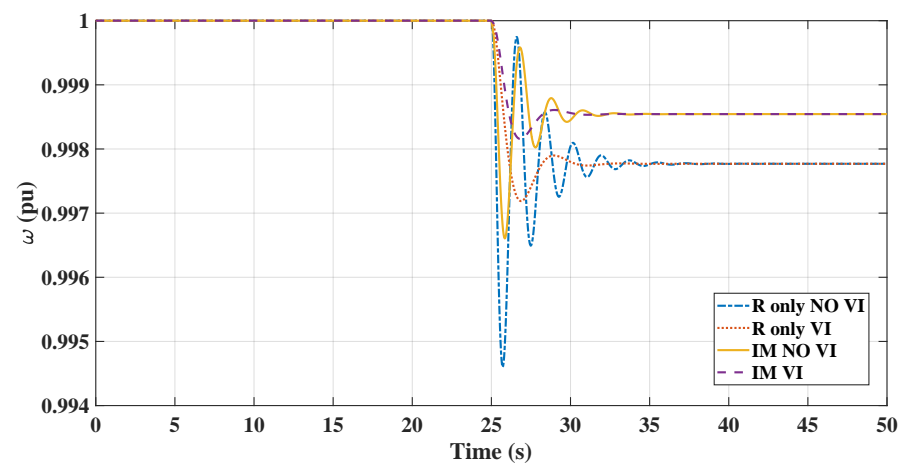|	R Only without VI	R Only with VI	IM without VI	IM with VI
Nadir	0.9946	0.9972	0.9966	0.9982
RoCoF	4.912/kS	1.496/kS	3.852 /kS	0.983

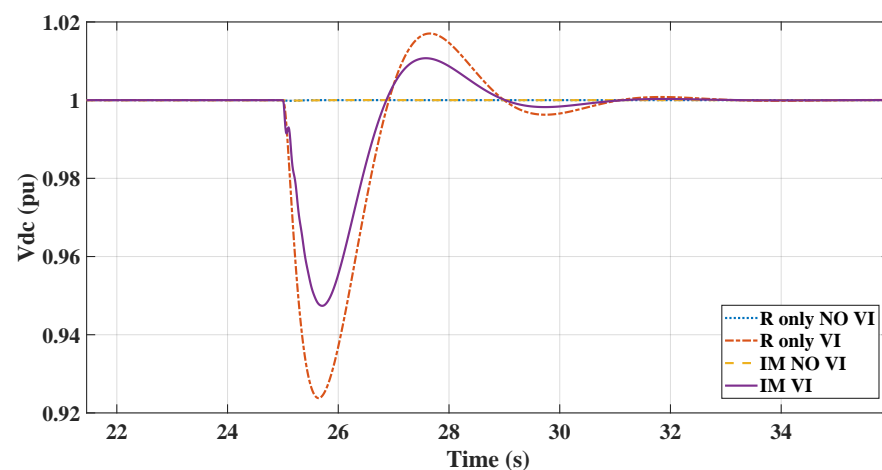**Figure 13.** Frequency response at different loading conditions.

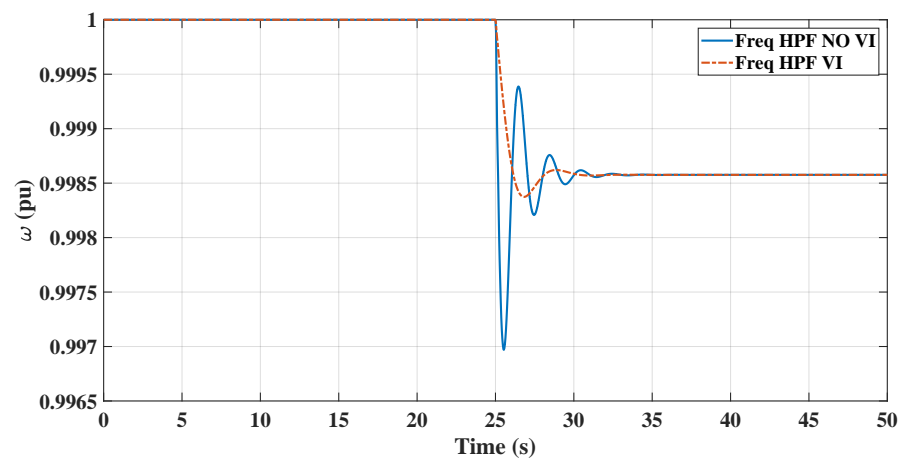**Figure 14.** DC bus voltage at different loading conditions.

Figure 15. Frequency response comparison when dynamic loads increased by 3%.

4.4. Effect of Network System Parameters

In this section, the effect of changing the system parameters is studied. The first parameter is the DC microgrid loading. The DC microgrid loading consists of two types of loads: constant power load, which is deducted from the constant power source that represents the renewable energy source, and the other type is the resistive load.

Figure 16 shows the frequency response at different DC resistive loading levels 0.25, 0.5 and 1MW. The constant power source is also varied to keep the power transfer between the DC microgrid and the AC microgrid at 0.5 MW for all cases. The system shows a more stable response and better inertia support when the loading level increased on the DC side. Figure 16 illustrates that the frequency response is enhanced by increasing the DC loading. The reason for this improved performance is the decrease in DC voltage during the contingency by the effect of the virtual inertia loop that also affects the power absorbed by the DC loads which leads to more available power to be transferred to the AC microgrid producing more inertial support and better frequency response, as shown in Figure 17. Figure 18 shows the DC bus voltage at the same loading condition when transferring the constant power from the DC to the AC microgrid. In Figure 19, the effect of changing the synchronous generator inertia on DC bus voltage is depicted under a 3% change in the dynamic load. As expected, the increase in the generator inertia leads to a more stable response in the DC bus voltage as it reduces the burden on the stored energy at the DC link for inertia support. Figure 20 shows the frequency response which is further improved at higher generator inertia.
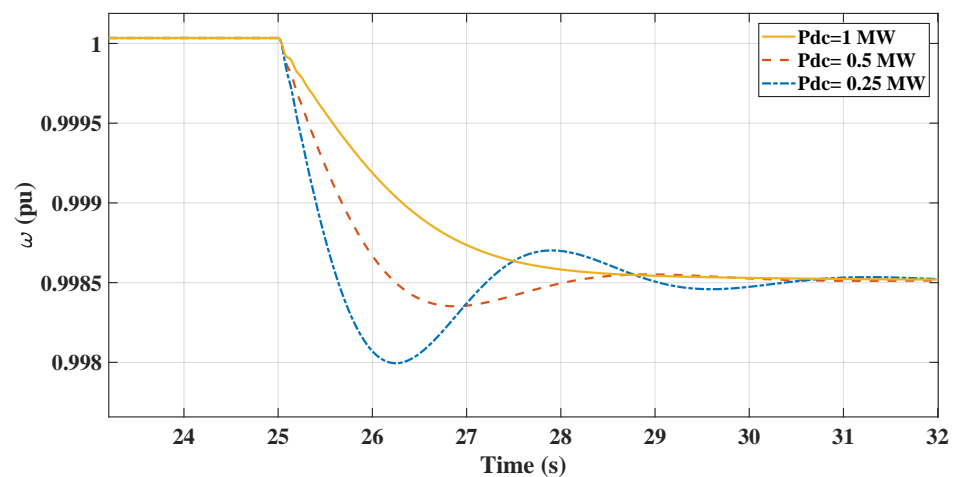

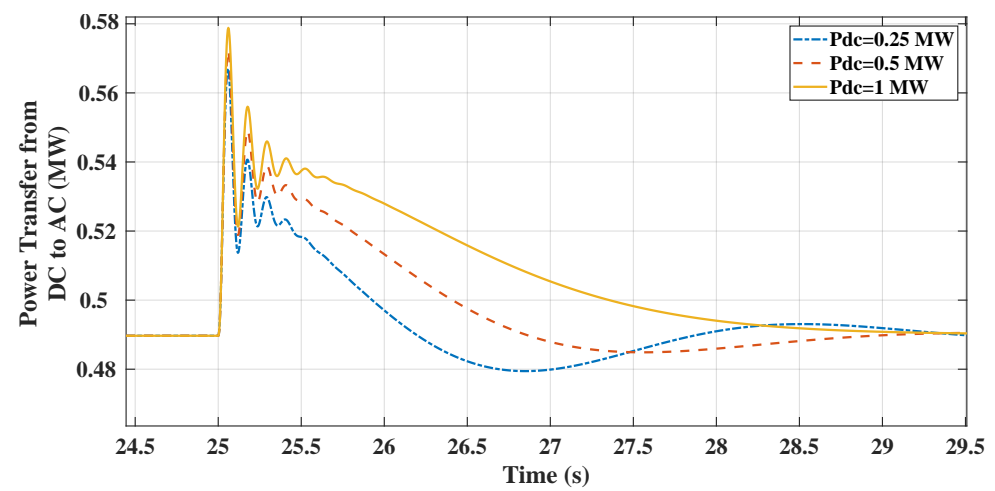**Figure 16.** Frequency Response at different DC-microgrid loadings.

Figure 17. Power transfer from DC to AC grid at different DC-microgrid loadings.
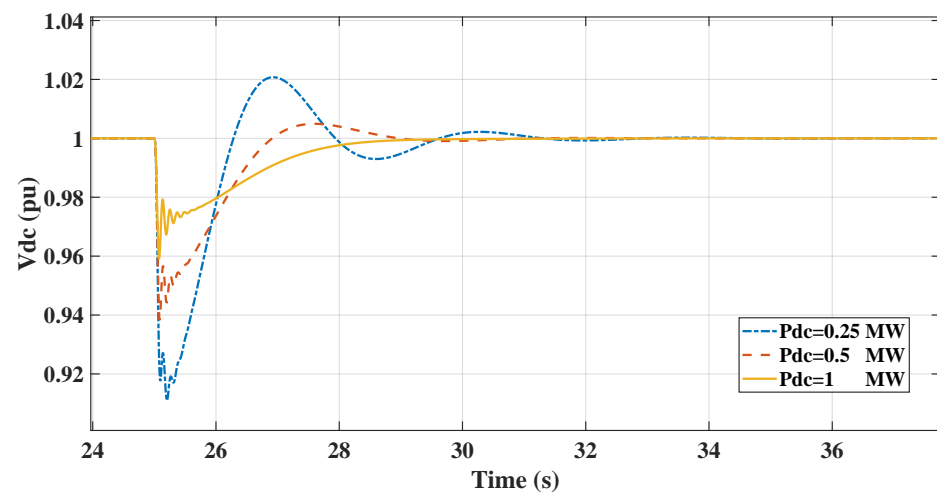

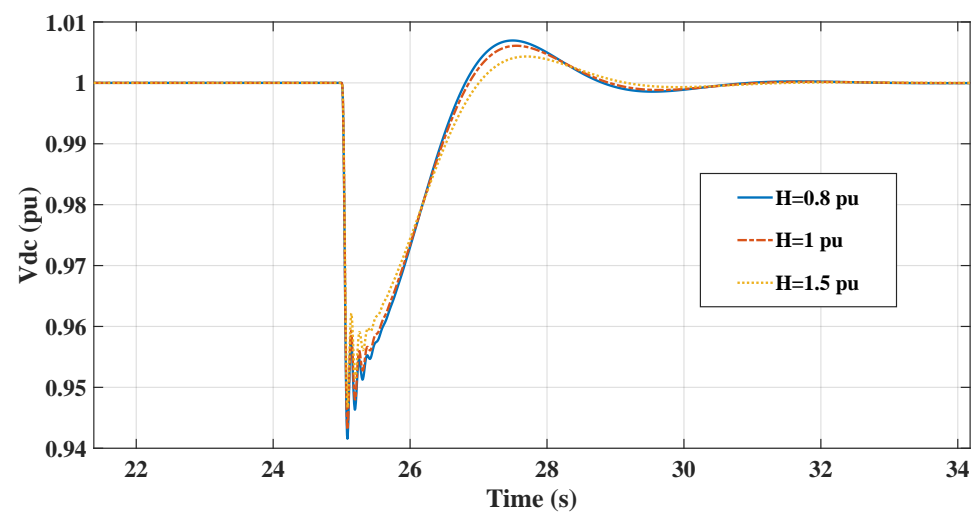**Figure 18.** DC bus voltage at different DC-microgrid loadings.

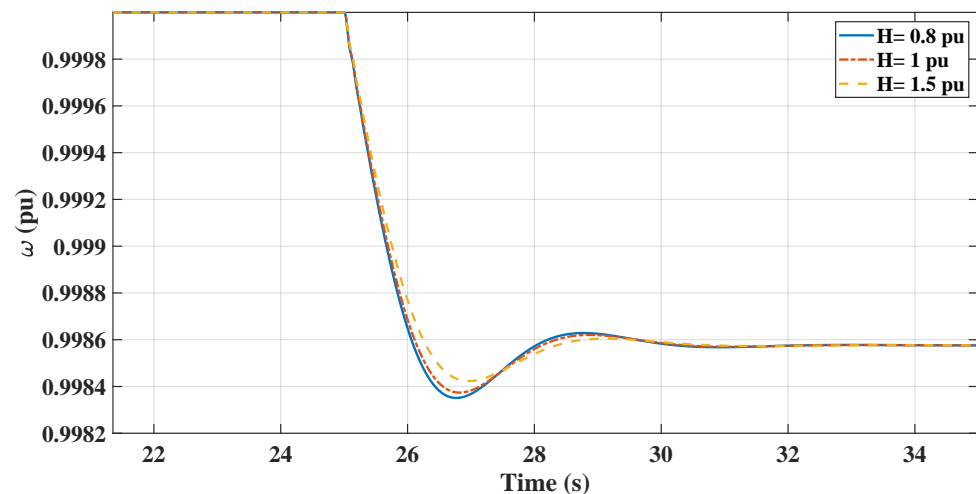**Figure 19.** DC bus voltage at different generator inertia.

Figure 20. Frequency Response at different generator inertia.

5. Conclusions

This paper presented a virtual inertia controller based on a high-pass filter compensator to facilitate providing DC grids with an inertial support to low-inertia AC grids. The control system's dynamic performance is tested using Matlab/Simulink software. The state-space linearized model of the system is developed and validated. It has been proved that the results of the linearized system coincide with those of the non-linear model, verifying the accuracy of the state-space model. The system's frequency response regarding RoCoF and Nadir is compared under different loading scenarios; it has been found that with the motor load connected, the system frequency showed better RoCoF and Nadir compared to the cases where only static loads are introduced. This is because the inertia of the rotating parts of the motors is added to the inertia of the synchronous generator. It has been shown that the virtual inertia controller would enhance the frequency response when activated and that the DC link voltage of the DC microgrid is successfully restored to the nominal value after the contingency. The dynamic performance of the proposed virtual inertia control loop based on the HPF compensator is compared with its LPF counterpart, offering good frequency support but resulting in steady state error in the DC link voltage. In addition, the effects of changing the system's parameters are examined using the state space model and the system's eigenvalues are presented. Future work will include comparing the proposed HPF-based controller with other novel control approaches in the domain of virtual inertia, considering field measurement data captured from the real systems based on the AC-DC microgrid concept.

Author Contributions: Conceptualization, A.M.I.M. and M.I.M.; methodology, A.M.I.M. and M.I.M.; software, A.M.I.M. and M.A.A.; validation, A.M.I.M. and M.A.A.; formal analysis, A.M.I.M. and M.A.A.; investigation, A.M.I.M., M.A.A. and M.I.M.; resources, A.M.I.M. and M.I.M.; data curation, A.M.I.M. and M.A.A.; writing-original draft preparation, M.A.A. and A.M.I.M.; writing-review and editing, A.M.I.M. and M.I.M.; visualization, A.M.I.M. and M.A.A.; supervision, A.M.I.M. and M.I.M.; project administration, A.M.I.M. and M.I.M.; funding acquisition, M.I.M. All authors have read and agreed to the published version of the manuscript.

References

1. Denholm, P.; Mai, T.; Kenyon, R.; Kroposki, B.; O'Malley, M. *Inertia and the Power Grid: A Guide Without the Spin*; Technical Report; National Renewable Energy Lab. (NREL): Golden, CO, USA, 2020.
2. Khazaei, J.; Tu, Z.; Liu, W. Small-signal modeling and analysis of virtual inertia-based PV systems. *IEEE Trans. Energy Convers.* **2020**, *35*, 1129–1138. [CrossRef]
3. Ratnam, K.; Kaliannan, P. Emulated Inertia Control for the Stand-Alone Microgrid with High Penetration of Renewable Energy Sources. *Int. J. Renew. Energy Res.* **2020**, *10*, 831.
4. Bašakarad, T.; Holjevac, N.; Kuzle, I.; Ivanković, I.; Zovko, N. Rocof Importance in Electric Power Systems with High Renewables Share: A Simulation Case for Croatia. In Proceedings of the 12th Mediterranean Conference on Power Generation, Transmission, Distribution and Energy Conversion (MEDPOWER 2020), Online, 9–12 November 2020.
5. Chen, T.; Guo, J.; Chaudhuri, B.; Hui, S.Y. Virtual inertia from smart loads. *IEEE Trans. Smart Grid* **2020**, *11*, 4311–4320. [CrossRef]
6. Ortega, Á.; Milano, F. Combined Frequency and RoCoF Control of Converter-Interfaced Energy Storage Systems. *IFAC-PapersOnLine* **2019**, *52*, 240–245. [CrossRef]
7. Saeedian, M.; Eskandari, B.; Taheri, S.; Hinkkanen, M.; Pouresmaeil, E. A control technique based on distributed virtual inertia for high penetration of renewable energies under weak grid conditions. *IEEE Syst. J.* **2021**, *15*, 1825–1834. [CrossRef]
8. Fang, J.; Li, H.; Tang, Y.; Blaabjerg, F. On the inertia of future more-electronics power systems. *IEEE J. Emerg. Sel. Top. Power Electron.* **2019**, *7*, 2130–2146. [CrossRef]
9. *946-2020*; IEEE Recommended Practice for the Design of DC Auxiliary Power Systems for Generating Stations, in IEEE Std 946-2020 (Revision of IEEE Std 946-2004). IEEE: Manhattan, NY, USA, 23 September 2020.
10. D'Arco, S.; Suul, J.A.; Fosso, O.B. A Virtual Synchronous Machine implementation for distributed control of power converters in SmartGrids. *Electr. Power Syst. Res.* **2015**, *122*, 180–197. [CrossRef]
11. Abuagreb, M.; Allehyani, M.F.; Johnson, B.K. Overview of Virtual Synchronous Generators: Existing Projects, Challenges and Future Trends. *Electronics* **2022**, *11*, 2843. [CrossRef]
12. Liu, Y.; Hao, M.; He, Y.; Zang, C.; Zeng, P. Review and Applications of Virtual Synchronous Machines Technologies. In Proceedings of the 2019 IEEE Innovative Smart Grid Technologies—Asia (ISGT Asia), Chengdu, China, 21–24 May 2019.
13. Pan, D.; Wang, X.; Liu, F.; Shi, R. Transient Stability of Voltage-Source Converters With Grid-Forming Control: A Design-Oriented Study. *IEEE J. Emerg. Sel. Top. Power Electron.* **2020**, *8*, 1019–1033. [CrossRef]
14. Fang, J.; Li, H.; Tang, Y.; Blaabjerg, F. Distributed power system virtual inertia implemented by grid-connected power converters. *IEEE Trans. Power Electron.* **2018**, *33*, 8488–8499. [CrossRef]
15. Rocabert, J.; Capo-Misut, R.; Munoz-Aguilar, R.S.; Candela, J.I.; Rodriguez, P. Control of Energy Storage System Integrating Electrochemical Batteries and Supercapacitors for Grid-Connected Applications. *IEEE Trans. Ind. Appl.* **2019**, *55*, 1853–1862. [CrossRef]
16. Zhang, M.; Liu, Y.; Li, D.; Cui, X.; Wang, L.; Li, L.; Wang, K. Electrochemical Impedance Spectroscopy: A New Chapter in the Fast and Accurate Estimation of the State of Health for Lithium-Ion Batteries. *Energies* **2023**, *16*, 1599. [CrossRef]
17. Abuagreb, M.; Abuhussein, A.; alZahir, S. Sizing of Energy Storage System for Virtual Inertia Emulation. In Proceedings of the 2022 IEEE 31st International Symposium on Industrial Electronics (ISIE), Anchorage, AK, USA, 1–3 June 2022.
18. Zhang, C.; Rakhshani, E.; Kumar, N.V.; Rueda-Torres, J.L.; Palensky, P.; Gonzalez-Longatt, F. Real-time simulation Model of Ultracapacitors for Frequency Stability Support from Wind Generation. In Proceedings of the IECON 2021—47th Annual Conference of the IEEE Industrial Electronics Society, Toronto, ON, Canada, 13–16 October 2021.
19. Hadavi, S.; Mansour, M.Z.; Bahrani, B. Optimal Allocation and Sizing of Synchronous Condensers in Weak Grids With Increased Penetration of Wind and Solar Farms. *IEEE J. Emerg. Sel. Top. Circuits Syst.* **2021**, *11*, 199–209. [CrossRef]
20. Mehrabankhomartash, M.; Saeedifard, M.; Yazdani, A. Adjustable wind farm frequency support through multi-terminal HVDC grids. *IEEE Trans. Sustain. Energy* **2021**, *12*, 1461–1472. [CrossRef]
21. Vennelaganti, S.G.; Chaudhuri, N.R. Stability criterion for inertial and primary frequency droop control in MTDC grids with implications on ratio-based frequency support. *IEEE Trans. Power Syst.* **2020**, *35*, 3541–3551. [CrossRef]
22. Wang, W.; Li, Y.; Cao, Y.; Hager, U.; Rehtanz, C. Adaptive droop control of VSC-MTDC system for frequency support and power sharing. *IEEE Trans. Power Syst.* **2018**, *33*, 1264–1274. [CrossRef]
23. Martinez Sanz, I.; Chaudhuri, B.; Strbac, G. Inertial response from offshore wind farms connected through DC grids. *IEEE Trans. Power Syst.* **2015**, *30*, 1518–1527. [CrossRef]
24. Zhu, J.; Booth, C.D.; Adam, G.P.; Roscoe, A.J.; Bright, C.G. Inertia emulation control strategy for VSC-HVDC transmission systems. *IEEE Trans. Power Syst.* **2013**, *28*, 1277–1287. [CrossRef]
25. Chen, D.; Xu, Y.; Huang, A.Q. Integration of DC microgrids as virtual synchronous machines into the AC grid. *IEEE Trans. Ind. Electron.* **2017**, *64*, 7455–7466. [CrossRef]
26. Yana, S.; James, A.F.; Emhemed, A.; Burt, G. Decentralised Control of DC Microgrid Based on Virtual Admittance to Enhance DC Voltage and Grid Frequency Support. In Proceedings of the 2018 53rd International Universities Power Engineering Conference (UPEC), Glasgow, UK, 4–7 September 2018.
27. Han, Y.; Li, H.; Shen, P.; Coelho, E.A.A.; Guerrero, J.M. Review of Active and Reactive Power Sharing Strategies in Hierarchical Controlled Microgrids. *IEEE Trans. Power Electron.* **2017**, *32*, 2427–2451. [CrossRef]

28. Florida-James, A.; Yana, S.; Emhemed, A.; Burt, G. Investigation of a decentralised control strategy for grid frequency support from DC microgrids. *J. Eng.* **2019**, *2019*, 5099–5103. [CrossRef]

29. AbuHussein, A.; Ingalls, N.; Sadi, M.A.H.; AbuAgreb, M. Transient Stability Microgrid Model for Arctic Community Integration. In Proceedings of the 2020 IEEE/PES Transmission and Distribution Conference and Exposition (T&D), Chicago, IL, USA, 12–15 October 2020.

30. Mohamad, A.M.E.I.; Mohamed, Y.A.R.I. Investigation and Assessment of Stabilization Solutions for DC Microgrid With Dynamic Loads. *IEEE Trans. Smart Grid* **2019**, *10*, 5735–5747. [CrossRef]

31. Kundur, P. *Power System Stability and Control*; McGraw-Hill Professional: New York, NY, USA, 1994.

32. Sauer, P.W.; Pai, M.A. *Power System Dynamics and Stability*; Pearson: Upper Saddle River, NJ, USA, 1997.

33. Mohamad, A.M.I.; Mohamed, Y.A.R.I. Analysis and Mitigation of Interaction Dynamics in Active DC Distribution Systems with Positive Feedback Islanding Detection Schemes. *IEEE Trans. Power Electron.* **2018**, *33*, 2751–2773. [CrossRef]